Novel Multicomponent Composite with TiO_2/Y_2O_3 as Cathode Material and Interlayer for Li-SPAN Batteries Cycled at High C-rates

Ana L. Páez Jerez , María L. Vera , Edgardo L. Sham , Alvaro Y. Tesio , Victoria Flexer

PII: S0013-4686(23)01051-4
DOI: https://doi.org/10.1016/j.electacta.2023.142876
Reference: EA 142876

To appear in: *Electrochimica Acta*

Received date: 5 April 2023
Revised date: 6 July 2023
Accepted date: 10 July 2023

Please cite this article as: Ana L. Páez Jerez , María L. Vera , Edgardo L. Sham , Alvaro Y. Tesio , Victoria Flexer , Novel Multicomponent Composite with TiO_2/Y_2O_3 as Cathode Material and Interlayer for Li-SPAN Batteries Cycled at High C-rates, *Electrochimica Acta* (2023), doi: https://doi.org/10.1016/j.electacta.2023.142876

Novel Multicomponent Composite with TiO_2/Y_2O_3 as Cathode Material and Interlayer for Li-SPAN Batteries Cycled at High C-rates

Ana L. Páez Jerez,[1] María L. Vera,[1] Edgardo L. Sham,[2] Alvaro Y. Tesio [1]* and Victoria Flexer[1]*

[1] Centro de Investigación y Desarrollo en Materiales Avanzados y Almacenamiento de Energía de Jujuy-CIDMEJu (CONICET-Universidad Nacional de Jujuy), Centro de Desarrollo Tecnológico General Savio, Palpalá, Jujuy 4612, Argentina.

[2] Instituto de Investigaciones para la Industria Química-INIQUI (CONICET- Universidad Nacional de Salta), Avda. Bolivia N° 5150, Salta, Salta 4400, Argentina.

*Corresponding authors: atesio@cidmeju.unju.edu.ar, vflexer@unju.edu.ar

Abstract

A novel multicomponent composite within the broad sulfurized polyacrylonitrile family of composites (SPAN) was synthesized. This innovative composite, termed as SPAN/Ti-Y, was composed of S, PAN, TiO_2 and Y_2O_3. Cathodes were made using a two-step coating technique, resulting in two regions with synergistic functions. The first region is built on the multicomponent composite while the second zone is prepared with the mixture of metal oxides only. The present work describes a different Li-SPAN cell, standing out for its third and fourth components of TiO_2/Y_2O_3 which accomplish two vital functions as both modifying the SPAN cathode material and as an interlayer between cathode and separator. An extensive morphological, structural and electrochemical characterization of the composite was performed. The content of S and TiO_2/Y_2O_3 was 40.6 % (29.9 % sulfur according to ICP-OES and elemental analysis, and 10.7 % TiO_2/Y_2O_3, according to TGA). Through XPS analysis of the as-synthesized composite and cells that underwent different number of cycles, a better understanding of the molecular structure can be suggested. When proved as cathode material, the cell reached capacity values of 1528 mAh g^{-1} for the 5^{th} cycle and 907 mAh g^{-1} after 850 cycles (results express per mass of S + TiO_2/Y_2O_3), with a capacity fading per cycle of 0.07 %, at 3 C in simple carbonate-based electrolytes. These values are superior that a SPAN cathode material with commercial TiO_2. Our results lead us to think that TiO_2 mixed with Y_2O_3 could act not only as a valuable second active component but also as an electrocatalyst, and the electrochemical reactions of sulfur could be combined with the insertion/extraction of lithium within the structure of TiO_2/Y_2O_3.

Keywords: SULFURIZED POLYACRYLONITRILE; METAL OXIDES; CATHODE MATERIAL; CATHODE INTERLAYER; Li-SPAN BATTERIES.

1. Introduction

Sulfurized polyacrylonitrile materials, commonly referred to as SPAN, have been intensively studied since their first report in 2002 and represent a very promising prospect for cathode material in the coming generation of energy storage systems: lithium-sulfur (Li-S) batteries.[1] Their exceptional performance is due to distinctive qualities that set them apart from the typical Li-S battery with S_8-containing cathodes.[2–5] One of the most notable differences is that SPAN cathodes feature a single sloped voltage plateau with a solid-solid mechanism since the sulfur is present in the form of short chains ($-S_n-$, $n \leq 4$) which are covalently bonded to the PAN backbone. This crucial characteristic removes the harmful shuttle effect and is applicable to both ether-based electrolytes, which are used in traditional Li-S batteries, and carbonate-based electrolytes, which are the common electrolytes used in Li-ion batteries.[6–12]

Different molecular structures for SPAN have been proposed and it is known that the sulfur content strongly depends on the binding sites for sulfur in the SPAN structure. [6,13–17] SPAN cathodes revealed capacity values beyond or close to the theoretical capacity of sulfur (1675 mAh g^{-1}) with an average sulfur content of 40 %.[6,18,19] However, when the discharge capacities are expressed by grams of composite, these values are less than or equal to 500 mAh g^{-1} due to the relatively low sulfur content by mass of composite.[6,19]

Taking advantage of the inherent characteristics of SPAN, adding a third compound to modify SPAN cathodes could be one of the options to enhance the electrochemical performance, leading to even longer cyclability, high specific capacity values and making possible their practical application in modern technologies. Wang *et al.* observed that adding CNT fibers to SPAN cathodes, a specific capacity of 1180 mAh g^{-1} sulfur (481 mAh g^{-1} composite) is obtained without capacity fading for more than 1000 cycles at 0.5 C with a sulfur content of 40.8 %.[18] Razzaq *et al.* designed SPAN fibers embedded in CNT/CoS_2 and CNT/Co with excellent performance for high energy density batteries in carbonate-based electrolytes.[20,21] SPAN cells with CNT/CoS_2 tested at a current density of 1 C and high mass loading, achieved a long-term cycling for 500 cycles. In turn, the cells prepared with CNT/Co reached a stable cycling for 1500 cycles at 1 C. He *et al.* found that a SPAN cell with CNT/Se reached stable cycling over 800 cycles at 1 C with a high reversible capacity of 622 mAh g^{-1} composite in carbonate-based electrolyte.[22]

The redox processes undergone by SPAN cathodes are heavily debated. Some authors claim there is a different behaviour in ether-based electrolytes when compared to carbonate-based electrolytes.[7] The majority of specialists suggest that Li_2S formation as the final discharge product or lack thereof in SPAN cathodes involves a one-step redox conversion.[13,15–18,23] In carbonate-based electrolytes, no soluble intermediate polysulfides (Li_2S_n, $n \leq 4$) were found, demonstrating superior electrochemical performance. However, the performance in ether electrolytes is inferior because of the high solubility of these intermediate polysulfides (Li_2S_{3-4}) in ether electrolytes, which restrict redox conversion and result in the unfavourable shuttle effect. It has been found that using eutectic accelerators such as Te and Se along with SPAN results in a faster redox conversion than polysulfide dissolution, as well as outstanding rate, long cycling performance and compatibility with ether-based electrolytes.[24–26]

Metal sulfides such as FeS and Ni_2S were also used to modify SPAN cathodes.[27,28] Better results were obtained with the former, where the authors designed a dual-active cathode material with high sulfur content (77.8 %) that depicted synergistic effects between FeS nanoparticles and SPAN fibers. The cell achieved a capacity value of 886 mAh g^{-1} sulfur (689 mAh g^{-1} composite) at 0.6 C for 500 cycles.[28] Metal oxides such as $Mg_{0.6}Ni_{0.4}O$ and commercial TiO_2 were also employed as additives in SPAN cathode materials. Although the electrochemical performance obtained with a ternary composite based on S, polyacrylonitrile and $Mg_{0.6}Ni_{0.4}O$ was informed only for 100 cycles at a low C-rate (0.1 C), it was performed at a high mass loading (4 mgS cm^{-2}).[29] In turn, the cathode obtained with TiO_2 worked at higher C-rate and developed long cycling at 3.3 C for over 250 cycles with an average discharge capacity of 932 mAh g^{-1} sulfur, although at lower mass loading and sulfur content.[30]

The two-step coating method is unique for producing cathode materials. It is a very effective substitute for producing an interlayer between the separator and cathode that prevents any potential migration of lithium polysulfides, towards the lithium anode, if any were to be produced. It has been shown that this strategy can improve the electrochemical performance of Li-S batteries, since interlayer components have the capacity to catalyse the polysulfide conversion and/or provide strong chemical and physical adsorption.[31–35] Besides, the high capacity of some metal oxides to adsorb and trap the polysulfides led to the observation that using Y_2O_3 to modify the cathode

and separator in classical Li-S batteries had a positive impact on the electrochemical performance.[36–38]

In this article, we present a novel multicomponent composite, denoted as SPAN/Ti-Y, composed of S, PAN, TiO_2 and Y_2O_3. SPAN/Ti-Y was thoroughly characterized from a morphological and chemical perspective to comprehend its structure and correlate it with the electrochemical performance. The cathode for Li-SPAN batteries was prepared via a two-step coating method, resulting in two distinctive regions with synergistic functions. The first region is built from the multicomponent composite, while the second zone is prepared with TiO_2/Y_2O_3/Super P. The present work describes a novel Li-SPAN cell, SPAN/Ti-Y/interlayer, standing out for its third and fourth components, TiO_2 and Y_2O_3. These accomplish two vital functions, modifying the classical SPAN cathode material and as an interlayer between cathode and separator. The electrochemical performance of the new composite when used as active cathode material in Li-S batteries was studied and compared with SPAN combined with commercial TiO_2. Our results showed that both S and TiO_2/Y_2O_3 function as active materials undergoing distinctive redox processes. The innovative cell with two regions (SPAN/Ti-Y/interlayer) and a content of S and TiO_2/Y_2O_3 of 40.6 % delivered a capacity value of 1528 mAh g^{-1} for the 5th cycle and stable capacity of 907 mAh g^{-1} after 850 cycles at 3 C in carbonate-based electrolytes (capacity values express per mass of S + TiO_2/Y_2O_3). To the best of our knowledge no SPAN composites, have previously been reported in combination with TiO_2/Y_2O_3, nor using the two-step coating approach.

2. Experimental Section

2.1 Preparation of TiO_2/Y_2O_3. The sol-gel method was used to prepare TiO_2/Y_2O_3. The solid modified with yttrium was synthesized using hydrated yttrium (III) acetate (Strem Chemicals, Inc.) as a precursor. This precursor was dissolved in water, which was slowly added dropwise to 1 M solution of titanium isopropoxide (Sigma-Aldrich) in isopropyl alcohol, under constant stirring. Then, the final solid was washed by centrifugation and dried at 65 ºC for 12 hours in static air, obtaining a white powder. The mixture of metal oxides, TiO_2/Y_2O_3, was calcined at 450 ºC for 1 hour in static air, in order to remove residual groups from the precursor alkoxide and obtain a specific crystalline phase.

2.2 Preparation of composite and interlayer. Sulfur powder (> 99 % Biopack), polyacrylonitrile (PAN, Polysciencies, Inc.) and the as-prepared TiO_2/Y_2O_3 particles were mixed in a mass ratio of 4:1:0.25 in ethanol by means of a planetary ball mill (RETSCH, PM 100) at 300 RPM for 3 hours (referenced as wet ball-milling in Figure 1). After the mechanical treatment, the mixture was subjected to a heating treatment at 350 °C for 6 hours under nitrogen atmosphere in a tubular furnace (Indef, T-150 model) to obtain SPAN/Ti-Y composite. The same process was used to synthesize a Control SPAN composite, but without the inclusion of TiO_2/Y_2O_3 particles.

In a similar procedure, commercial titanium dioxide (TiO_2 anatase, Carlo Erba Reagents S.A., analytical quality for analysis grade, > 98.5%. The main impurities specified by the supplier are chloride (<200 ppm), Fe (<50 ppm) and Zn (<50 ppm). No Y content is declared), polyacrylonitrile (PAN), and sulfur were combined in a mass ratio of 0.25:1:4 using a planetary ball mill for 3 hours at 300 RPM. After the mechanical treatment, the mixture underwent a heating procedure in a tubular furnace at 350 °C for 6 hours under nitrogen atmosphere. The resulting ternary composite, SPAN/Ti, was a black powder.[30]

The interlayer material was prepared following the method reported by Zeng *et al*.[34] Firstly, 0.3 g of carbon Super P was added to 50 mL of ethanol and dispersed by ultrasound for 1 h. Then 0.2 g of TiO_2/Y_2O_3 was added to the solution, ultrasonicated for 15 more minutes, followed by magnetic stirring for 30 min to make it evenly mixed. The product was collected through filtration and fully dried at 100 °C in a vacuum oven (ARCANO DZF60-20) for its later use.

2.3 Composite material characterization. Sulfur content was determined by elemental analysis (Carlo Erba EA 1108 elemental analyser) and by inductively coupled plasma-optical emission spectrometry (ICP-OES, Shimadzu 9000). Thermogravimetric Analysis (TGA) was performed in a Thermogravimetric Analyzer (TGA-50, SHIMADZU) from room temperature to 700 °C under O_2 atmosphere and from room temperature to 600 ºC under N_2 atmosphere, both at a heating rate of 10 °C min^{-1}. X-ray diffraction (XRD) patterns were recorded with a PHILIPS PW1710 X-ray diffractometer with copper anode and curved graphite monochromator, operating at 45 KV and 30 mA. The scanning conditions for structural analysis were recorded over a 2Θ range from 10° to 90°. The Raman spectrum was collected with a LabRAM HR Evolution Microscope (Horiba) using an excitation line of 532 nm in a range of 4850-100 cm^{-1}. The IR spectrum was performed with a FTIR spectrometer (JASCO 4600) in a range of 4000-450 cm^{-1}. X-ray photoelectron

spectroscopy (XPS) spectra of the as-synthesized composite and the cells charged after 1 cycle and discharged after 1, 2 and 500 cycles were recorded with Thermo Scientific K-Alpha X-ray Photoelectron Spectrometer. Previously, the cells were disassembled, and the same solvent mixture used to prepare the electrolyte was used to wash the cathodes. Morphological analysis and elemental mapping of the SPAN/Ti-Y composite were performed by Field Emission Scanning Electron Microscopy (FE-SEM) and Energy-dispersive X-ray spectroscopy (EDS), Carl Zeiss-Sigma. N_2 adsorption–desorption isotherms at 77 K were measured using a micromeritics adsorption equipment (ASAP 2000). Previously, samples were degassed at 170 ◦C for 12 h. The specific surface areas (S_{BET}) were obtained by means of the BET (Brunauer, Emmet and Teller) equation. The pore size distributions and medium pore diameter were determined using the Density Functional Theory (DFT). The micropore volumes ($V_{\mu P}$) were obtained by α-plot model and the total volumes of porous (V_{TP}) by Gurvich's rule at a relative pressure of 0.98.

2.4 Cathode preparation. A two-step coating procedure was implemented to prepare the electrodes (see Figure 1). First, the synthesized multicomponent composite, SPAN/Ti-Y, carbon Super P (GELON LIB GROUP, type C45), and PAN (also utilized as a binder)[39–41] were blended in a mass ratio of 80:10:10. All components were dispersed in N-methyl-2-pyrrolidone (NMP, Sigma-Aldrich). The resultant slurry was uniformly spread onto an Al foil (GELON LIB GROUP) by doctor blade technique (Gelon, GN-VC-15H) and subsequently dried in a vacuum oven (ARCANO DZF60-20) at 60 °C for at least 12 hours. Following drying, a second slurry made of the interlayer material, TiO_2/Y_2O_3/carbon Super P and PAN (90:10) in NMP, was applied to the previously coated Al foil. It was then once more dried before being mechanically punched (Gelon-CP20) to create discs with a diameter of 12 mm. The cathode mass loading was 1 mg cm^{-2} and the interlayer mass loading was 0.45 mg cm^{-2} calculated based on TiO_2/Y_2O_3/carbon Super P (equivalent to 0.18 mg cm^{-2} based on TiO_2/Y_2O_3 content only).

A similar procedure was used to prepare cathodes made of SPAN-Ti, except that these cathodes did not contain an interlayer. Cathodes made of SPAN-Ti also had a mass loading of 1 mg cm^{-2}.

2.5 Electrochemical characterization. Electrochemical tests were performed in coin-type cells (CR 2032) with a lithium metal disc as anode (diameter of 15.6 mm and thickness of 0.45 mm), and polypropylene as separator (Celgard 2400, diameter of 16 mm and thickness of 25 μm), all components from GELON LIB GROUP. Coin-type cells were assembled in a glove box

(MBRAUN Unilab Pro SP) with H_2O and O_2 contents bellow 1 ppm and 0.1 ppm, respectively. The electrolyte used (40 µL) was 1 M lithium bis (trifluoromethanesulfonyl) imide (LiTFSI, > 99%, Sigma-Aldrich) dissolved in a solvent mixture of ethylene carbonate (EC), dimethyl carbonate (DMC) and diethylene carbonate (DEC) with a volume ratio of 4:2:4 (Gelon). The water content of the electrolyte solution determined by Karl Fischer Coulometer (Metrohm) was 11.5 ppm. All electrochemical measurements were carried out in an 8-channel lithium battery tester analyzer (Neware). The cells were discharged and charged galvanostatically (GDC) at different current rates (C-rates) between 1 and 3 V at room temperature. For SPAN-Ti-Y, specific capacities and current densities were calculated based, alternatively, on the content of sulfur and TiO_2/Y_2O_3 (40.64 %) and the mass of composite. For SPAN-Ti, specific capacities and current densities were calculated based, alternatively, on the content of sulfur and TiO_2 (41.1 %), and the mass of composite. GDC tests of current collectors coated with the mixture of metal oxides and commercial TiO_2 were performed at 0.1 A g^{-1}. Cyclic voltammetry (CV) was measured in a VMP3 BioLogic multichannel galvanostat-potentiostat at a scan rate of 0.1 mV s^{-1} between 1 V and 3 V.

3. Results and Discussion

3.1 Structural, morphological, and chemical characterizations of TiO_2/Y_2O_3

The mixture of metal oxides (TiO_2/Y_2O_3), synthesized by sol-gel technique and subsequently calcined, and the commercial sample of TiO_2 were thoroughly characterized and results were compared (see Figure 2). TiO_2/Y_2O_3 had 2.49 % Y_2O_3, according to analytical electron microscope run by EDS. The XRD pattern detected TiO_2 in the majority polymorphic variety of anatase for both commercial TiO_2 and TiO_2/Y_2O_3. The average crystal size observed by SEM was 200 nm for TiO_2/Y_2O_3. The S_{BET} value for TiO_2/Y_2O_3 was 120 m^2 g^{-1}, while the S_{BET} value obtained for commercial TiO_2 was 10 m^2 g^{-1}. The results from XRD were corroborated by Raman spectra, which only showed peaks corresponding to the three E_g modes (642, 199, and 148 cm^{-1} for TiO_2/Y_2O_3 and 639, 196, and 142 cm^{-1} for commercial TiO_2), a doublet of the A_{1g} and B_{1g} modes (518 cm^{-1} for TiO_2/Y_2O_3 and 514 cm^{-1} for commercial TiO_2), and the B_{1g} mode (399 cm^{-1} for TiO_2/Y_2O_3 and 396 cm^{-1} for commercial TiO_2) that are attributable to the anatase phase of TiO_2.[42] No Y_2O_3 was detected by XRD or Raman. Additionally, the most intense peak of Y_2O_3 is entangled with the B_{1g} mode of anatase TiO_2, making it very challenging to detect well-dispersed solid mixtures. Although XRD and Raman could not detect the presence of Y_2O_3, SEM using a

backscattered electron detector was able to identify a compositional contrast in the mixture of metal oxide (see Figure S.1), confirming the results from EDS.

3.2 Structural, morphological, and chemical characterizations of SPAN/Ti-Y composite

The sulfur content for SPAN/Ti-Y composite was 28.9 % determined by ICP-OES. Whereas the elemental analysis determined 11.9 % N, 31.9 % C, 2.5 % H, and 30.9 % S. The average value of the two techniques was 29.9 % S. The structural characterization of SPAN/Ti-Y is shown in Figure 3. TGA assessed the content of TiO_2/Y_2O_3 in SPAN/Ti-Y (10.7 %, calculation is given in TGA calculations in S.I.), which added to 29.9 % S, resulted in a total active material content of 40.6 % (value used for normalizing electrochemical results). Results were contrasted with those of a Control SPAN sample, which lacked TiO_2 or TiO_2/Y_2O_3. As shown in Figure 3 a, elemental sulfur exhibited a unique weight loss taking place between 200 and 330 °C. Meanwhile, PAN depicted two weight losses: one at 300 °C and the other one at temperatures higher than 300 °C. TiO_2/Y_2O_3 exhibited a small weight loss of 3.5 % in the studied temperature range, therefore it could be considered thermally stable in the analysed temperature range. SPAN/Ti-Y displayed two weight losses: one in the range of 240-350 °C and the second one from 350 to 650 °C. The initial weight loss may be attributed to S-S bonds or unreacted sulfur, while the second weight loss could be attributed to C-S bonds. This presumption is consistent with Control SPAN and other SPAN studies reported in the literature.[14,23] It can also be seen that there is no further degradation of Control SPAN after 700 °C, with a remaining residue of 9.7 %.

The crystal phase of the as-prepared SPAN/Ti-Y multicomponent composite was investigated using XRD analysis. SPAN/Ti-Y is definitely not a completely amorphous structure as shown in Figure 3 b. The XRD spectrum showed several peaks associated with anatase TiO_2 (A) and carbon (C), but no crystalline peaks of elemental sulfur. This implied that there was no remaining elemental sulfur in the composite and confirms the formation of short-chain organosulfides that bound to the carbon framework. The XRD spectra were quite similar when compared to those of SPAN/Ti in our previous findings.[30] Anatase TiO_2 (A) peaks could also be seen in the spectrum of SPAN/Ti. Most crystalline peaks observed in Figure 2 a still remained after synthesis treatment in both composites, the mixture metal oxides and commercial TiO_2. Characteristic peaks of Y_2O_3 at 2 theta angles = 29, 34, 49 and 58° are not identified in SPAN/Ti-Y composite. Y_2O_3 is present in a concentration less than the resolution limit of the equipment. Contrasting our findings with

those of the rest of SPAN, without the addition of a third or fourth component, where a typical disordered graphite-like structure is seen,[22–24,26,28] our spectra were distinctly different.

The FTIR and Raman spectra for SPAN/Ti-Y revealed highly similar structural information (see Figures 3 c and d). Neither of the spectra showed bands for TiO_2 nor for Y_2O_3, which characteristic band should have appeared at 560 cm^{-1}. Therefore, it could be said that the addition of TiO_2/Y_2O_3 did not alter the classical SPAN structure of this new multicomponent composite. The set of bands located at 1600-1100 cm^{-1} (IR) and the band at 802 cm^{-1} (IR) could be attributed to the formation of six-membered rings owning C=C and C=N bonds. The G (carbon-bond stretching in the graphite plane) and D (carbon-bond breathing in disordered carbon) modes appeared at 1542/1535 cm^{-1} (IR/Raman) and 1357/1320 cm^{-1} (IR/Raman), respectively. The defect level in carbon materials is determined by the relative intensity ratio I_D/I_G.[43] The greater the I_D/I_G, the greater the defect level. The I_D/I_G value for SPAN/Ti-Y was 0.93, slightly lower than that obtained for SPAN/Ti (I_D/I_G = 0.98), indicating a slightly higher degree of order for SPAN/Ti-Y. The peaks at 1162 (IR) and 934 cm^{-1} (IR) are assigned to ring breathing of a side-chain containing S-S and C-S bonds. The peak located at 934 cm^{-1} could be assigned to the combination of C-S bonds and also N-S bonds which is in agreement with that observed by Huang *et al*.[17] Another group of bands that evidence the formation of C-S bonds are located at 663 cm^{-1} (IR) and 405 cm^{-1} (Raman). The set of bands accounting for the anatase phase of TiO_2 are located at 615, 405, 152 and 202 cm^{-1} in the Raman spectrum, in agreement with the Raman spectrum in Figure 2 b.[42,44] We can therefore conclude that our multicomponent composite has a structure that is at least comparable to that found for the classical SPAN family because they both share the same bands. These peak assignments are all in line with recent literature reports.[22–24,28,30]

The morphology and elemental mapping of SPAN/Ti-Y was investigated by SEM and EDS mapping and they are depicted in Figure 4. The SEM images show the particles are in a circular-shape and these aggregate into a bulky cluster. The EDS elemental mapping revealed that the carbon elemental mapping images overlapped with sulfur, oxygen and titanium mapping images, strongly suggesting the homogeneous distribution of all elements in SPAN/Ti-Y composite. Yttrium was once again unidentified. This lack of identification could be brought on by the low yttrium content both in TiO_2/Y_2O_3 and the final composite.

Figure 5 displays the results of an XPS study of the SPAN/Ti-Y multicomponent composite and SPAN/Ti-Y/interlayer cells at various charge and discharge cycles. This section will address the examination of the high-resolution C 1s, N 1s, S 2p, and Ti 1s of solely the as-synthesized composite (see Figure 5 a). The C 1s XPS spectrum of the composite showed a band which could be split into three peaks located at 284.9, 285.9 and 287.2 eV. The first two signals can be assigned to C-C/C-H/C=C bonds and the last one to C=N/C-N/C-S bonds.[8,23,28,45] N 1s XPS spectrum can be deconvoluted into three peaks located at 399.1, 400.5 and 401.6 eV. These three contributions correspond to pyridinic N (~398 eV), pyrrolic N (~400 eV) and graphitic N (≥400 eV), respectively. Therefore, it could be assumed that the SPAN structure is composed by a combination of pyridinic, pyrrolic and graphitic N.[13,22,28,45] S 2p XPS spectrum displayed four contributions located at 162.7, 164.5, 165.9 and 169.8 eV. The peak at 162.7 eV could be attributed to single C-S bonds.[15,26,45] Moreover, the region at ~162 eV could also be ascribed to Ti-S bond, suggesting an interaction between Ti with S.[46,47] The peak appeared at 164.5 eV is consistent with C-S/S-S bond in short-chain organic sulfur.[15,45] Meanwhile the peaks at 165.9 and 169.8 eV can be assigned to S-N/S-S bonds and sulfates, respectively. Although this last signal is only observed in SPAN cathodes cycled.[12,16,48] Ti 2p XPS spectrum can be divided into two peaks at 459.8 and 465.5 eV which are representative of the Ti^{4+} oxidation state in TiO_2.[46,49] This region is also characteristic of Ti-S bonds, making reference to a strong physical adsorption of polysulfides in the surface of TiO_2 nanoparticles[46,50,51] and/or sulfur incorporated into TiO_2 lattice, forming S-Ti-O bonds.[52] The proximity of the Y 3d bands to S 2p bands may lead them to be obscured. The signals from the yttrium oxides are between 155 and 159 eV, while the signal from S 2p is between 163 and 164 eV (S_8 or S).[53] Consequently, since the sulfur content is higher than the content of metal oxides (2.49 % Y_2O_3 in the mixture of metal oxides), the sulfur signal will be stronger than the Y 3d signal and will mask it.

The combined results from IR, Raman, elemental analysis and XPS studies may indicate a feasible SPAN/Ti-Y structure, and Figure 6 illustrates such possibility. The collection of signals pointed to a cyclic structure with backbones of =C-N-C and C-NH-C, in which sulfur was covalently bound to both carbon and nitrogen atoms in short chains. The structure suggested by Huang *et al.* could also apply to our multicomponent composite.[13,17] Additionally, as IR or Raman bands for S-Ti-O were not seen, the main interactions between Ti and S observed, point to a physical adsorption. The Raman peak at 202 cm^{-1} could be indicative of this physical interaction due to a

slight shift of the E_g mode observed at 199 cm^{-1} in the Raman spectrum of TiO_2/Y_2O_3. The polymer matrix and metal oxide particles appeared to be completely homogeneously dispersed, according to EDS elemental mapping. One may argue that sulfur is present in SPAN/Ti-Y in two ways, either as chemical interactions or as physical interactions between all of the components: covalently bound in short chains to the SPAN matrix or adsorbed to TiO_2/Y_2O_3 particles.

3.3 Electrochemical performance

With the aim to comprehend the performance of SPAN/Ti-Y/interlayer cell, its electrochemical properties were studied. In order to understand its redox peaks, the CV tests are carried out for the first and second cycles for SPAN/Ti-Y/interlayer and they were compared with those obtained for our cathode material reported before, SPAN/Ti [30] and the current collector coated with TiO_2/Y_2O_3. Two reduction peaks and two oxidation peaks are already visible in SPAN/Ti-Y/interlayer for the first cycle at potentials of 1.50 and 1.70 V and 2.00 and 2.30 V, respectively, as seen in Figure 7 a. The reduction peak at 1.50 V, moves to higher potential for the second cycle, appearing at 2.01 V, and it is attributed to the reduction of the low order polysulfides to the Li_2S (Figure 7 b). Meanwhile the oxidation peak at 2.30 V corresponds to the reverse process.[9,54] For the cell using commercial TiO_2, in the first cycle only one reduction and one oxidation peaks are observed, in marked contrast with the CV curve of SPAN/Ti-Y/interlayer. The second cycle of the cell with commercial TiO_2 shows two reduction peaks at similar potentials than SPAN/Ti-Y/interlayer, but still only one oxidation peak, i.e. still a different profile than the multicomponent CV profile. From the second to fifth cycles of the cell using SPAN/Ti-Y/interlayer, there were only slight variations for both the anodic and cathodic CV peaks, indicating exceptional cycling stability and weak polarization (see Figure S.2).

As we mentioned before, SPAN cathodes feature a single sloped voltage plateau since sulfur was identified to be present in the form of short chains which are covalently bonded to the PAN backbone.[6,7,55] Therefore, one reduction peak and one oxidation peak should be observed. In order to distinguish if some of the other peaks observed in the CV curves correspond to the redox processes of TiO_2/Y_2O_3, we performed the CV tests for this mixture of metal oxides and compared results with commercial TiO_2 at 0.1 mV/s (see Figure 7 c). It can be concluded that the peaks at 1.70 and 2.00 V in Figures 7 a and b correspond to the reduction and oxidation processes of TiO_2.[30,56,57] We could think that the shoulders at 1.45 and 1.84 V in Figures 7 a and b could

be attributed to the reduction and oxidation processes of Y_2O_3, since these are absent in commercial TiO_2. However, these two shoulders, which were also observed by Li and co-workers, were reported by some organized anatase nanostructures.[58] In addition, the anodic peak of commercial TiO_2 is weak while the reduction peak is strong, maybe it is the reason for which the oxidation peak is not observed in the CV curves for SPAN/Ti.

The peaks at 1.70 and 2.00 V were already observed in other studies and were attributed to the lithiation and delithiation of anatase TiO_2.[44,56,57,59,60] Therefore, the redox process of TiO_2 (eq. 1) are added to the redox reaction of Li-SPAN batteries:[56]

$$TiO_2 + x\ e^- + x\ Li^+ \longleftrightarrow Li_xTiO_2\ (0 < x < 1) \qquad \text{(eq. 1)}$$

We may infer from this assertion and the results of the CV tests that the solid-solid SPAN mechanism in our SPAN/Ti-Y cathodes also involves the lithiation/delithiation of TiO_2, which in our case may be supplying additional capacity. At this point, there are two different options. According to some authors, the inherent Li-insertion in TiO_2 contributes very little to the overall capacity.[57,61] Equation 1 translates to a theoretical capacity of 168 mAh g^{-1} for x = 0.5 at a formal potential of 1.85 V vs. Li^+/Li.[57,62–64] Figure 8 shows 110 mAh g^{-1}, in relatively good agreement with the theoretical capacity. Additionally, the increase in capacity values is minimal when taking into account the concentration of TiO_2 in the cathode. Li *et al.*, on the other hand, looked into the electrochemical functionality of TiO_2/CNTs in the context of rechargeable lithium batteries.[58] They found that the electrochemical performance is highly dependent on the loading of TiO_2, and the conductivity of the CNTs may also influence the efficiency of the cell. The irreversible capacity loss in the first cycle occurs often. But at low TiO_2 loading, the capacity just slightly decreases from the third to the fifteenth cycle, showing good cycling stability. Contrarily, cell performance declines noticeably when TiO_2 content rises, possibly as a result of electrode pulverization and a challenge with lithium diffusion brought on by particle agglomeration. The TiO_2/Y_2O_3 utilized in this study outperformed other TiO_2/Y_2O_3 mixtures that were similarly made using the sol-gel method (see Figure S.3), and it had a fairly stable capacity across 100 cycles, which is comparable to what Li *et al.* observed.[58]

Moreover, it can be clearly seen that the performance obtained with the mixture of metal oxides is much better than commercial TiO_2 (see Figure 8). For the first 10 cycles, the capacity value of the

mixture is roughly 2.5 that of commercial TiO_2. A much more stable cycling is also observed, resulting in 4 times higher capacity value after 100 cycles when the mixture is compared to commercial TiO_2. More importantly, TiO_2/Y_2O_3 provides extra capacity in the same voltage window of SPAN and is a highly reversible redox couple.

Following results in Figure 8, we speculate that in combination with SPAN, TiO_2/Y_2O_3 could provide additional reversible capacity and aid in the efficiency and/or stability of the cell. This would be in line with results reported by Li *et al.*[58] Another mechanism that might take place in our cell is a surface-mediated reduction up to Li_2S on the metal oxides surface. As a result, the metal oxides, which serve as an active electrode material, contributes to the sulfur redox chemistry .[57] The boost in electrochemical performance seen in our cell may be due to the combination of these two mechanisms.

Since SPAN/Ti-Y/interlayer cell contains two redox couples that work as active electrode materials and might provide reversible capacity, the theoretical capacity of SPAN/Ti-Y composite is 1326 mAh g^{-1} (normalization by grams of S and metal oxides, see Supplementary Table 1). The rate capability studies for SPAN/Ti-Y/interlayer and SPAN/Ti showed high sulfur utilization and high capacity values, increasing C-rate from 0.15, 0.30, 0.75, 1.00 and 1.50 C and returning back to 0.15 C (1 C = 1326 mAh g^{-1}, we recall the mass refers to S + TiO_2/Y_2O_3, see Figure 9). For a better comparison of the rate capability studies for SPAN/Ti-Y/interlayer and SPAN/Ti with capacity values and C-rates expressed by gram of sulfur, see Figure S.4, where current values are also expressed in A g^{-1} units. In addition, both cells demonstrated better electrochemical performance than a cell without any metal oxide, i.e. composed of Control SPAN only.[30] SPAN/Ti-Y/interlayer and SPAN/Ti were able to keep stable cycling for 10 cycles as the cycling rates increased and the recovering percentages of their initial capacities were 86 and 78 % for SPAN/Ti-Y/interlayer and SPAN/Ti, respectively. Most importantly, SPAN/Ti-Y/interlayer showed superior capacity values for all the range of C-rates under study (26 % higher at 0.15 C, and 28 % higher at 1.50 C). In the graph, we can also see higher capacity values than the theoretical capacity of SPAN/Ti-Y (1326 mAh g^{-1}). The same was observed by Haridas *et al.*, who found that the combined SPAN and FeS capacities were 250 mAh g^{-1} greater than the theoretical capacity of SPAN. The authors speculated that the conjugated pyridinic carbon of SPAN may have contributed

to this increased capacity.[28] In our case, the extra capacity could also be attributed to the interlayer (see Figure S.5).

The cycling performance of SPAN/Ti-Y/interlayer at 0.45 C (0.6 A g^{-1}) was similarly compared with a cell without Y_2O_3, SPAN/Ti cell. The SPAN/Ti-Y/interlayer cell reached a capacity value of 896 mAh g^{-1} S&TiO_2/Y_2O_3 after 600 cycles (0.09 % capacity fading per cycle) and a coulombic efficiency close to 100 %, except for the first cycle (see Figure 10 a). The differences between SPAN/Ti-Y/interlayer and SPAN/Ti are much more remarkable at higher current density (3.00 C, 3.9 A g^{-1}, see Figure 10 b): 34 - 41% higher capacity for SPAN/Ti-Y/interlayer. The SPAN/Ti-Y/interlayer cell reached capacity values of 1528 and 907 mAh g^{-1} S&TiO_2/Y_2O_3 for the 5^{th} and after 850 cycles, respectively, with a capacity fading of 0.07 % per cycle, yielding an overall capacity retention of 59 % after 850 cycles. The capacity fading was almost identical at 0.45 and 3.00 C.

All the electrochemical analysis show that the combination of TiO_2 with Y_2O_3 and the creation of an interlayer have a beneficial effect on the cells' capacity, the cycling stability and galvanostatic discharge/charge tests at high C-rates. A beneficial effect of Y_2O_3 as a modifying agent was previously observed in the structure of cathode materials in lithium-ion batteries, and other energy storage devices such as supercapacitors and solar cells.[65–69] In addition, in photocatalytic applications, an improvement in the photocatalytic efficiency with the introduction of the dopant yttrium ion in similar compounds was reported.[70–73] Firstly, this can be due to yttrium ions producing an increase in the specific surface area and higher microporosity. Secondly, yttrium ions can act as electron traps,[72] which would aim not only the separation of the electron-hole pair but also electron transfer to the oxygen molecule adsorbed on the titania surface that acts as an electron acceptor. Finally, yttrium ions can prevent the recombination of the electron-hole pair, increasing the half-life of the charge carriers, so that they can participate in photocatalytic processes.[73]

3.4 XPS analysis of the charged and discharged cells

Finally, with the objective to further understand the excellent electrochemical properties of SPAN/Ti-Y/interlayer and correlate the redox mechanism to the molecular structure, XPS analysis of SPAN/Ti-Y/interlayer cathodes cycled at 0.15 C after 1 discharge cycle, 1 charge cycle, 2 discharge cycles and 500 discharge cycles are discussed (see Figure 5 b-e).

The region between 283 and 285 eV is where C-C/C=C/C-H bonds correspond to the binding energies; the peak position will vary depending on the chemical environment in which they are found. Slight shifts of such bonds can be distinguished in the cycled cathode. The signal observed at lower binding energies (~283 eV) in the cathodes after 1 charge cycle and discharged after 500 cycles could also be attributed to carbides.[33] The peaks assigned to C=N/C-N/C-S bond widened and decreased in intensity as the battery is cycled, being almost imperceptible after 500 cycles compared with the as-synthesized composite spectrum, which could indicate an almost totally lithiated state. Two new bands were identified in the cathode cycled after 1 discharge cycle, appearing at 288.7 and 291.8 eV. O-C=O could be responsible for the first signal and poly(CO_3)/delocalized electrons/CF_2 for the second.[12,23,74] The presence of carbonates is due to the formation of the cathode-electrolyte interphase (CEI) derived from reactions between cathode and electrolyte components with the aim to form a protective layer. Besides, it is important to note that the signal attributed to CF_2 grows significantly when the cycling increases. The existence of fluorine is confirmed by analysing the survey spectra in the 680-690 eV region (see Figure S.6). This signal was not observed in the as-synthesized composite, while the presence of fluorine is clearly appreciated in the rest of the cathodes cycled.

With regard to N 1s spectra, three contributions can be observed for both composite and cathodes cycled, except for the cathodes charged and discharged after 500 cycles. These three contributions from low to high binding energy correspond to pyridinic, pyrrolic and graphitic N. Wu *et al.* assigned the contribution at higher eV to a positively charged nitrogen atom ($–N^+$).[46] In Figure 5, an important increase in the graphitic N or $–N^+$ signal for the cathodes discharged after 1 and 2 cycles can be seen. Wu and co-workers noted that N-H bonds play an important role on polysulfides chemisorption during charge/discharge conversion. Therefore, it is reasonable to think that pyrrolic N signals decreased due to the cleavage of the N-H bonds while $–N^+$ signals increased due to the formation of N-Li-S bonds, detecting the pyridinic N as the unique signal for both the cathodes charged and discharged after 500 cycles.

Analysing the S 2p spectra, new peaks located at 161.2 and 160.5 eV were detected in the cathodes discharged after 1 and 2 cycles, respectively, which were assigned to Li_2S/Li_2S_2 discharge products.[15,16,23,28] This signal appeared after 1 discharge cycle and vanished after charging, demonstrating the excellent reversibility of the cell. Besides, the same Li_2S/Li_2S_2 signal was not

discerned for the cathode discharged after 500 cycles. This is in agreement with data reported by Shen *et al.*, who studied the cathode-electrolyte interphase (CEI), determining that as the cycling progresses, the CEI consisted of mainly LiF, dominating the inorganic phase and carbonates in the organic phase.[74] The signals appeared at approximately 167, 168 and 169 eV could be ascribed to sulfites, thiosulfates and sulfates, respectively.[16,23,46] The cathode discharged after 500 cycles is dominated by the sulfite peak while those discharged after 1 and 2 cycles are dominated by the most oxidized species, thiosulfates and sulfates. In the charged cathode, the lithium polysulfide signal disappeared and a new signal at 159.4 eV appeared, which could be attributed to yttrium.

With regards to Ti 2p spectrum, there are some variation in the measurements registered, e.g. number scan and acquisition time, which make it difficult to reach accurate conclusions. The as-synthesized composite was measured with 6 scans while the cell charged after 1 cycle and the discharged cells were measured using 35 and 3 scans, respectively. Another point to consider is the fact that titanium is one of the minor elements along with yttrium in the multicomponent composite, and since the CEI is deposited on the cathode surface as it cycles, it is very likely that the signal stops being detected when the cycle number increases. Therefore, if we analysed the spectrum for the as-synthesized composite and the cathode after 1 cycle of charge, the number of scans was incremented by a factor of 5.83 and the signal becomes noisy. This is indicative of a change in the surface that covers partially the titanium signal. So probably, after various cycles of charge/discharge, the signal of this element could be lost. Unfortunately, it cannot be confirmed due to the difference in scans. Another explanation for the lack of Ti 2p signals in the discharged cathode spectra could be the mechanism outlined by Kavan and colleagues.[57] With a surface-enhanced redox chemistry, they saw a sulfur reduction that was facilitated on titania. Due to the polysulfides that are produced after discharging, which may have adsorbed on the surface of TiO_2, the Ti 2 p signals may be obscured by them. The two Ti-O signals registered for the as-synthesized composite were down-shifted after charge, appearing at 456.8 and 465.5 eV. Huang *et al.* indicated that such a shift is due not only to chemical interactions between sulfur and TiO_2, but also electron donation from sulfides to TiO_2.[46,47,75]

The signal of Li 1s is obviously absent in the as-synthesized composite. It appears after discharge and it is shifted from higher to lower binding energies when the number of discharge cycles

increases, with binding energy values of 55.7, 55.3 and 54.1 for the 1st, 2nd and after 500th discharge cycles, respectively. Whereas, the signal is up-shifted by 1 eV (56.7 eV) for the charged cathode with regards to that discharged after 1 cycle. Shen and co-workers attributed the region of 54-56 eV to $ROCO_2Li/LiCO_3$ and the region higher than 56 eV to LiF.[74] It is in accordance with the formation/modification of the CEI. It has been shown that during the initial cycles, lithium species change from LiF to oxygenated species before becoming carboxylated species, which is the primary component of the CEI. The latter is consistent with what our spectrum revealed. According to Sun *et al.* shifts of Li 1 s to lower binding energy revealed that Li is gaining electron density upon its interaction with Ti species and sulfur.[50]

After all this analysis, it is possible to suggest a redox mechanism in SPAN/Ti-Y/interlayer. Previously, we stablished that our multicomponent composite was formed by pyridinic and pyrrolic rings where sulfur is bonded to not only carbon atoms but also nitrogen atoms. Besides, sulfur can be found in the form of short-chains and it is interacting with Ti. After 1st discharge, SPAN/Ti-Y underwent dramatic changes and did not recover to its original state, i.e. the as-synthesized composite. The short-chain S-S bonds were broken and the pyrrolic N intensity dropped. The lithiation process and CEI creation provide an explanation for these alterations. We can see that Li_2S is formed in the first discharge state as a final product, which is in agreement with other reports.[15,23] However, Huang *et al.* noticed comparable alterations in their in-situ Raman investigations of SPAN cathodes, with the primary exception being that they did not detect any lithium polysulfide or Li_2S. Instead, the authors suggested a single lithiation process for SPAN that results in an ordered Li_2S-cPAN structure (c refers to carbonized). Lithium is then removed from the SPAN structure by a subsequent delitiathion process.[17] Maybe our SPAN/Ti-Y/interlayer batteries also experienced the redox mechanism observed by Huang. The following would be the suggested redox process for our system:

$$TiO_2 + x\ e^- + x\ Li^+ \longleftrightarrow Li_xTiO_2\ (0 < x < 1) \quad \text{(eq. 1)}$$

$$SPAN/Ti\text{-}Y + x\ e^- + x\ Li^+ \longleftrightarrow SPAN/Ti\text{-}Y + Li_2S \quad \text{(eq. 2) and/or}$$

$$SPAN/Ti\text{-}Y + x\ e^- + x\ Li^+ \longleftrightarrow Li_2SPAN/Ti\text{-}Y \quad \text{(eq. 3)}$$

High resolution XPS spectra after the 1st charge and the subsequent 2nd discharge were highly comparable to those after the 1st discharge, demonstrating good reversibility and stability of

SPAN/Ti-Y/interlayer. However, due to the formation of an almost fully lithiated SPAN/Ti-Y structure, the XPS spectra of the cell discharged after 500 cycles were considerably different from those of the 1st discharge. Another point to be considered is that after the 1st discharge/charge cycle, SPAN/Ti-Y/interlayer did not come back to the as-synthesized composite, therefore we can think that there is an activation process and/or structural change, not fully understood, similar to that observed by Wang[16] and Huang.[17]

Therefore, it could be said that the excellent electrochemical performance of our cathodes stems from an activation process, resulting in an optimized structure that endures through consecutive cycles; the formation of a protective and stable CEI. The presence of covalent N-S and C-S bonds and the combination of pyrrolic and pyridinic nitrogen in the structure of our novel multicomponent composite, is believed to own the ability of anchoring polysulfides and Li_2S.[76–78] We suggest that there is a strong synergistic effect between the lithiation/delitiation process of the TiO_2 and the solid-solid mechanism of SPAN. If the final discharge product, Li_2S, was formed in our system, it should be interacting with the metal oxides and the interlayer, enhancing the stability and cycling of our innovative multicomponent cell. We also demonstrate that the interlayer of TiO_2/Y_2O_3/Super P between the cathode and separator is essential for improving the performance of the battery, particularly for high C-rates, high capacity values, and lengthy cycling.

4. Conclusions

A novel multicomponent composite was synthesized, characterized and tested as cathode material in Li-SPAN cells. A mixture of metal oxides, TiO_2/Y_2O_3, was used to modify not only the cathode material but also to create an interlayer between cathode and separator, remarkably improving the cycling stability, cells' capacity values and C-rates of the cell. To the best of our knowledge, SPAN/Ti-Y is amongst the extremely few composites within the large SPAN family for which long lasting cyclability (more than 300 cycles) at high charge-discharge rates (3 C or higher) has been demonstrated. The fact that SPAN/Ti-Y multicomponent composite contained carbon, clearly visible in the XRD spectrum, increased the conductivity and decreased the polarization of the cell, allowing for improved kinetics and the cycling of the cells at high C-rates. Throughout the XPS analysis of the both the as-synthesized and cycled cells, the polymeric structure could be better

understood and the important role that the pyrrolic N and the mixture of metal oxides play on the chemisorption of the polysulfides in the redox conversion is demonstrated. Results presented here highlight the great benefits of employing TiO_2/Y_2O_3 as both an interlayer and cathode material component, and it presents a workable and promising strategy that opens the door to enhanced energy storage systems.

Acknowledgment

MLV acknowledges a CONICET post-doctoral fellowship. ALPJ, ELS, VF and AYT are CONICET permanent research fellows. This work was supported by ANPCyT, grant PICT-2020-03351, and CONICET, grant PIP-11220200100704CO). Sistema Nacional de Microscopías (AR) is acknowledged for the FE-SEM, EDS and XPS determinations.

References

[1] J. Wang, J. Yang, J. Xie, xu naixin, A Novel Conductive Polymer-Sulfur Composite Cathode Material for Rechargeable Lithium Batteries, Adv. Mater. 14 (2002) 963–965.

[2] S. Yao, Y. He, Y. Wang, M. Bi, Y. Liang, A. Majeed, Z. Yang, X. Shen, Porous N-doped carbon nanofibers assembled with nickel ferrite nanoparticles as efficient chemical anchors and polysulfide conversion catalyst for lithium-sulfur batteries, J. Colloid Interface Sci. 601 (2021) 209–219. https://doi.org/10.1016/j.jcis.2021.05.125.

[3] S. Yao, C. Zhang, F. Xie, S. Xue, K. Gao, R. Guo, X. Shen, T. Li, S. Qin, Hybrid Membrane with SnS_2 Nanoplates Decorated Nitrogen-Doped Carbon Nanofibers as Binder-Free Electrodes with Ultrahigh Sulfur Loading for Lithium Sulfur Batteries, ACS Sustain. Chem. Eng. 8 (2020) 2707–2715. https://doi.org/10.1021/acssuschemeng.9b06064.

[4] C. Zhang, Y. He, Y. Wang, Y. Liang, A. Majeed, Z. Yang, S. Yao, X. Shen, T. Li, S. Qin, $CoFe_2O_4$ nanoparticles loaded N-doped carbon nanofibers networks as electrocatalyst for enhancing redox kinetics in Li-S batteries, Appl. Surf. Sci. 560 (2021) 149908. https://doi.org/10.1016/j.apsusc.2021.149908.

[5] S. Yao, M. Bi, H. Yu, C. Zhang, X. Zhang, H. Liu, T. Zhang, J. Xiang, X. Shen, Spinel manganese-cobalt oxide nanospheres anchored on nitrogen-containing carbon nanofibers as a highly efficient redox electrocatalyst in lithium/polysulfides batteries, Appl. Surf. Sci. 598

(2022) 153787. https://doi.org/10.1016/j.apsusc.2022.153787.

[6] X. Zhao, C. Wang, Z. Li, X. Hu, A. Abdul Razzaq, Z. Deng, Sulfurized polyacrylonitrile for high-performance lithium sulfur batteries: advances and prospects, J. Mater. Chem. A. 9 (2021) 19282–19297. https://doi.org/10.1039/d1ta03300j.

[7] R. Mukkabla, M.R. Buchmeiser, Cathode materials for lithium-sulfur batteries based on sulfur covalently bound to a polymeric backbone, J. Mater. Chem. A. 8 (2020) 5379–5394. https://doi.org/10.1039/c9ta12619h.

[8] M.A. Weret, C.F. Jeffrey Kuo, T.S. Zeleke, T.T. Beyene, M.C. Tsai, C.J. Huang, G.B. Berhe, W.N. Su, B.J. Hwang, Mechanistic understanding of the Sulfurized-Poly(acrylonitrile) cathode for lithium-sulfur batteries, Energy Storage Mater. 26 (2020) 483–493. https://doi.org/10.1016/j.ensm.2019.11.022.

[9] S.S. Zhang, Sulfurized carbon: A class of cathode materials for high performance lithium/sulfur batteries, Front. Energy Res. 1 (2013) 1–9. https://doi.org/10.3389/fenrg.2013.00010.

[10] J. Wang, Y.S. He, J. Yang, Sulfur-based composite cathode materials for high-energy rechargeable lithium batteries, Adv. Mater. 27 (2015) 569–575. https://doi.org/10.1002/adma.201402569.

[11] Z. Li, L. Yuan, Z. Yi, Y. Sun, Y. Liu, Y. Jiang, Y. Shen, Y. Xin, Z. Zhang, Y. Huang, Insight into the electrode mechanism in lithium-sulfur batteries with ordered microporous carbon confined sulfur as the cathode, Adv. Energy Mater. 4 (2014) 1–8. https://doi.org/10.1002/aenm.201301473.

[12] Z. Wu, S.M. Bak, Z. Shadike, S. Yu, E. Hu, X. Xing, Y. Du, X.Q. Yang, H. Liu, P. Liu, Understanding the Roles of the Electrode/Electrolyte Interface for Enabling Stable Li‖Sulfurized Polyacrylonitrile Batteries, ACS Appl. Mater. Interfaces. 13 (2021) 31733–31740. https://doi.org/10.1021/acsami.1c07903.

[13] C.J. Huang, K.Y. Lin, Y.C. Hsieh, W.N. Su, C.H. Wang, G. Brunklaus, M. Winter, J.C. Jiang, B.J. Hwang, New Insights into the N-S Bond Formation of a Sulfurized-

Polyacrylonitrile Cathode Material for Lithium-Sulfur Batteries, ACS Appl. Mater. Interfaces. 13 (2021) 14230–14238. https://doi.org/10.1021/acsami.0c22811.

[14] S.S. Zhang, Understanding of sulfurized polyacrylonitrile for superior performance lithium/sulfur battery, Energies. 7 (2014) 4588–4600. https://doi.org/10.3390/en7074588.

[15] Z.Q. Jin, Y.G. Liu, W.K. Wang, A.B. Wang, B.W. Hu, M. Shen, T. Gao, P.C. Zhao, Y.S. Yang, A new insight into the lithium storage mechanism of sulfurized polyacrylonitrile with no soluble intermediates, Energy Storage Mater. 14 (2018) 272–278. https://doi.org/10.1016/j.ensm.2018.04.013.

[16] W. Wang, Z. Cao, G.A. Elia, Y. Wu, W. Wahyudi, E. Abou-Hamad, A.H. Emwas, L. Cavallo, L.J. Li, J. Ming, Recognizing the Mechanism of Sulfurized Polyacrylonitrile Cathode Materials for Li-S Batteries and beyond in Al-S Batteries, ACS Energy Lett. 3 (2018) 2899–2907. https://doi.org/10.1021/acsenergylett.8b01945.

[17] C.J. Huang, J.H. Cheng, W.N. Su, P. Partovi-Azar, L.Y. Kuo, M.C. Tsai, M.H. Lin, S. Panahian Jand, T.S. Chan, N.L. Wu, P. Kaghazchi, H. Dai, P.M. Bieker, B.J. Hwang, Origin of shuttle-free sulfurized polyacrylonitrile in lithium-sulfur batteries, J. Power Sources. 492 (2021) 229508. https://doi.org/10.1016/j.jpowsour.2021.229508.

[18] X. Wang, Y. Qian, L. Wang, H. Yang, H. Li, Y. Zhao, T. Liu, Sulfurized Polyacrylonitrile Cathodes with High Compatibility in Both Ether and Carbonate Electrolytes for Ultrastable Lithium–Sulfur Batteries, Adv. Funct. Mater. 29 (2019) 1–12. https://doi.org/10.1002/adfm.201902929.

[19] M.S. Ahmed, S. Lee, M. Agostini, M.G. Jeong, H.G. Jung, J. Ming, Y.K. Sun, J. Kim, J.Y. Hwang, Multiscale Understanding of Covalently Fixed Sulfur–Polyacrylonitrile Composite as Advanced Cathode for Metal–Sulfur Batteries, Adv. Sci. 8 (2021) 1–34. https://doi.org/10.1002/advs.202101123.

[20] A. Abdul Razzaq, X. Yuan, Y. Chen, J. Hu, Q. Mu, Y. Ma, X. Zhao, L. Miao, J.H. Ahn, Y. Peng, Z. Deng, Anchoring MOF-derived CoS_2 on sulfurized polyacrylonitrile nanofibers for high areal capacity lithium-sulfur batteries, J. Mater. Chem. A. 8 (2020) 1298–1306. https://doi.org/10.1039/c9ta11390h.

[21] A. Abdul Razzaq, G. Chen, X. Zhao, X. Yuan, J. Hu, Z. Li, Y. Chen, J. Xu, R. Shah, J. Zhong, Y. Peng, Z. Deng, Cobalt coordination with pyridines in sulfurized polyacrylonitrile cathodes to form conductive pathways and catalytic M-N_4S sites for accelerated Li-S kinetics, J. Energy Chem. 61 (2021) 170–178. https://doi.org/10.1016/j.jechem.2021.01.012.

[22] R. He, Y. Li, S. Wei, H. Liu, S. Zhang, N. Han, H. Liu, X. Wang, X. Zhang, Construction of high-performance sulfurized poly(acrylonitrile) cathodes for lithium-sulfur batteries via catalytic and conductive regulation, J. Alloys Compd. 919 (2022) 165838. https://doi.org/10.1016/j.jallcom.2022.165838.

[23] S. Wei, L. Ma, K.E. Hendrickson, Z. Tu, L.A. Archer, Metal-Sulfur Battery Cathodes Based on PAN-Sulfur Composites, J. Am. Chem. Soc. 137 (2015) 12143–12152. https://doi.org/10.1021/jacs.5b08113.

[24] X. Chen, L. Peng, L. Wang, J. Yang, Z. Hao, J. Xiang, K. Yuan, Y. Huang, B. Shan, L. Yuan, J. Xie, Ether-compatible sulfurized polyacrylonitrile cathode with excellent performance enabled by fast kinetics via selenium doping, Nat. Commun. 10 (2019) 1–9. https://doi.org/10.1038/s41467-019-08818-6.

[25] M. Jiang, K. Wang, S. Gao, R. Wang, J. Han, J. Yan, S. Cheng, K. Jiang, Selenium as Extra Binding Site for Sulfur Species in Sulfurized Polyacrylonitrile Cathodes for High Capacity Lithium-Sulfur Batteries, ChemElectroChem. 6 (2019) 1365–1370. https://doi.org/10.1002/celc.201801816.

[26] S. Li, Z. Han, W. Hu, L. Peng, J. Yang, L. Wang, Y. Zhang, B. Shan, J. Xie, Manipulating kinetics of sulfurized polyacrylonitrile with tellurium as eutectic accelerator to prevent polysulfide dissolution in lithium-sulfur battery under dissolution-deposition mechanism, Nano Energy. 60 (2019) 153–161. https://doi.org/10.1016/j.nanoen.2019.03.023.

[27] Y. Liu, W. Wang, A. Wang, Z. Jin, H. Zhao, Y. Yang, A polysulfide reduction accelerator-NiS_2-modified sulfurized polyacrylonitrile as a high performance cathode material for lithium-sulfur batteries, J. Mater. Chem. A. 5 (2017) 22120–22124. https://doi.org/10.1039/c7ta04279e.

[28] A.K. Haridas, J. Heo, Y. Liu, H.J. Ahn, X. Zhao, Z. Deng, M. Agostini, A. Matic, K.K. Cho, J.H. Ahn, Boosting High Energy Density Lithium-Ion Storage via the Rational Design of an FeS-Incorporated Sulfurized Polyacrylonitrile Fiber Hybrid Cathode, ACS Appl. Mater. Interfaces. 11 (2019) 29924–29933. https://doi.org/10.1021/acsami.9b09026.

[29] Y. Zhang, Y. Zhao, A. Yermukhambetova, Z. Bakenov, P. Chen, Ternary sulfur/polyacrylonitrile/$Mg_{0.6}Ni_{0.4}O$ composite cathodes for high performance lithium/sulfur batteries, J. Mater. Chem. A. 1 (2013) 295–301. https://doi.org/10.1039/c2ta00105e.

[30] A.L. Paez Jerez, L. Davies, A.Y. Tesio, V. Flexer, Synergistic Combination of TiO_2 and S-PAN for Li-S Batteries with Long-Term Cyclability at High C-Rates, J. Electrochem. Soc. 168 (2021) 120536. https://doi.org/10.1149/1945-7111/ac42a3.

[31] Y.S. Su, A. Manthiram, A new approach to improve cycle performance of rechargeable lithium–sulfur batteries by inserting a free-standing MWCNT interlayer, Chem. Commun. 48 (2012) 8817–8819. https://doi.org/10.1039/c2cc33945e.

[32] J. Fang, F. Qin, J. Li, K. Zhang, W. Liu, M. Wang, F. Yu, L. Zhang, Improved performance of sulfur cathode by an easy and scale-up coating strategy, J. Power Sources. 297 (2015) 265–270. https://doi.org/10.1016/j.jpowsour.2015.06.153.

[33] Y. An, Z. Zhang, H. Fei, S. Xiong, B. Ji, J. Feng, Ultrafine TiO_2 Confined in Porous-Nitrogen-Doped Carbon from Metal-Organic Frameworks for High-Performance Lithium Sulfur Batteries, ACS Appl. Mater. Interfaces. 9 (2017) 12400–12407. https://doi.org/10.1021/acsami.6b16699.

[34] P. Zeng, M. Chen, J. Luo, H. Liu, Y. Li, J. Peng, J. Li, H. Yu, Z. Luo, H. Shu, C. Miao, G. Chen, X. Wang, Carbon-Coated Yttria Hollow Spheres as Both Sulfur Immobilizer and Catalyst of Polysulfides Conversion in Lithium-Sulfur Batteries, ACS Appl. Mater. Interfaces. 11 (2019) 42104–42113. https://doi.org/10.1021/acsami.9b13533.

[35] G. Ma, Z. Wen, Q. Wang, C. Shen, P. Peng, J. Jin, X. Wu, Enhanced performance of lithium sulfur battery with self-assembly polypyrrole nanotube film as the functional interlayer, J. Power Sources. 273 (2015) 511–516. https://doi.org/10.1016/j.jpowsour.2014.09.141.

[36] M. Zhang, L. Peng, Q. Yuan, L. Zheng, Y. Wang, A. Li, A multifunctional separator modified using Y_2O_3/Co_3O_4 heterostructures boosting polysulfide catalytic conversion for advanced Li-S batteries, Sustain. Energy Fuels. 6 (2022) 3187–3194. https://doi.org/10.1039/d2se00479h.

[37] Z. Ding, X. Li, P. Zhang, J. Yu, Y. Hua, Enhanced electrochemical performance of sulfur on Y_2O_3-modified porous carbon aerogels for high performance lithium-sulfur batteries, New J. Chem. 41 (2017) 12726–12735. https://doi.org/10.1039/c7nj02714a.

[38] Y. Wang, H. Yu, A. Majeed, X. Shen, S. Yao, T. Li, S. Qin, Yttrium oxide nanorods as electrocatalytic polysulfides traps for curbing shuttle effect in lithium-sulfur batteries, J. Alloys Compd. 891 (2022) 162074. https://doi.org/10.1016/j.jallcom.2021.162074.

[39] L. Wang, X. He, J. Li, J. Gao, J. Guo, C. Jiang, C. Wan, Analysis of the synthesis process of sulphur-poly(acrylonitrile)-based cathode materials for lithium batteries, J. Mater. Chem. 22 (2012) 22077–22081. https://doi.org/10.1039/c2jm30632h.

[40] A.L. Páez Jerez, D.M. Chemes, E.L. Sham, L.E. Davies, A.Y. Tesio, V. Flexer, Low-Temperature Synthesis of a Sulfur-Polyacrylonitrile Composite Cathode for Lithium-Sulfur Batteries, ChemistrySelect. 5 (2020) 5465–5472. https://doi.org/10.1002/slct.202001529.

[41] L. Wang, X. He, W. Sun, J. Li, J. Gao, G. Tian, J. Wang, S. Fan, Organic polymer material with a multi-electron process redox reaction: Towards ultra-high reversible lithium storage capacity, RSC Adv. 3 (2013) 3227–3231. https://doi.org/10.1039/c3ra21187h.

[42] T. Ohsaka, F. Izumi, Y. Fujiki, Raman spectrum of anatase, TiO_2, J. Raman Spectrosc. 7 (1978) 321–324. https://doi.org/10.1002/jrs.1250070606.

[43] A.Y. Tesio, J.L. Gómez-Cámer, J. Morales, A. Caballero, Simple and Sustainable Preparation of Nonactivated Porous Carbon from Brewing Waste for High-Performance Lithium–Sulfur Batteries, ChemSusChem. 13 (2020) 3439–3446. https://doi.org/10.1002/cssc.202000969.

[44] N. Moreno, Á. Caballero, J. Morales, E. Rodríguez-Castellón, Improved performance of electrodes based on carbonized olive stones/S composites by impregnating with

mesoporous TiO_2 for advanced Li-S batteries, J. Power Sources. 313 (2016) 21–29. https://doi.org/10.1016/j.jpowsour.2016.02.061.

[45] J. Xiang, Z. Guo, Z. Yi, Y. Zhang, L. Yuan, Z. Cheng, Y. Shen, Y. Huang, Facile synthesis of sulfurized polyacrylonitrile composite as cathode for high-rate lithium-sulfur batteries, J. Energy Chem. 49 (2020) 161–165. https://doi.org/10.1016/j.jechem.2020.01.037.

[46] J. Wu, S. Li, P. Yang, H. Zhang, C. Du, J. Xu, K. Song, S@TiO_2 nanospheres loaded on PPy matrix for enhanced lithium-sulfur batteries, J. Alloys Compd. 783 (2019) 279–285. https://doi.org/10.1016/j.jallcom.2018.12.316.

[47] J.Q. Huang, Z. Wang, Z.L. Xu, W.G. Chong, X. Qin, X. Wang, J.K. Kim, Three-Dimensional Porous Graphene Aerogel Cathode with High Sulfur Loading and Embedded TiO_2 Nanoparticles for Advanced Lithium-Sulfur Batteries, ACS Appl. Mater. Interfaces. 8 (2016) 28663–28670. https://doi.org/10.1021/acsami.6b10032.

[48] X. Xing, Y. Li, X. Wang, V. Petrova, H. Liu, P. Liu, Cathode electrolyte interface enabling stable Li–S batteries, Energy Storage Mater. 21 (2019) 474–480. https://doi.org/10.1016/j.ensm.2019.06.022.

[49] Z. Cui, J. Yao, T. Mei, S. Zhou, B. Hou, J.J. Li, J.J. Li, J. Wang, J. Qian, X. Wang, Strong lithium polysulfides chemical trapping of TiC-TiO_2/S composite for long-cycle lithium-sulfur batteries, Electrochim. Acta. 298 (2019) 43–51. https://doi.org/10.1016/j.electacta.2018.12.075.

[50] K. Sun, Q. Zhang, D.C. Bock, X. Tong, D. Su, A.C. Marschilok, K.J. Takeuchi, E.S. Takeuchi, H. Gan, Interaction of TiS_2 and Sulfur in Li-S Battery System , J. Electrochem. Soc. 164 (2017) A1291–A1297. https://doi.org/10.1149/2.1631706jes.

[51] S. Ivanov, A. Barylyak, K. Besaha, A. Bund, Y. Bobitski, R. Wojnarowska-Nowak, I. Yaremchuk, M. Kus-Liśkiewicz, Synthesis, Characterization, and Photocatalytic Properties of Sulfur- and Carbon-Codoped TiO_2 Nanoparticles, Nanoscale Res. Lett. 11 (2016). https://doi.org/10.1186/s11671-016-1353-5.

[52] H. Li, X. Zhang, Y. Huo, J. Zhu, Supercritical preparation of a highly active S-doped TiO_2

photocatalyst for methylene blue mineralization, Environ. Sci. Technol. 41 (2007) 4410–4414. https://doi.org/10.1021/es062680x.

[53] D. Majumdar, D. Chatterjee, X-ray photoelectron spectroscopic studies on yttria, zirconia, and yttria-stabilized zirconia, J. Appl. Phys. 70 (1991) 988–992. https://doi.org/10.1063/1.349611.

[54] A. Rafie, J.W. Kim, K.K. Sarode, V. Kalra, A review on the use of carbonate-based electrolytes in Li-S batteries: A comprehensive approach enabling solid-solid direct conversion reaction, Energy Storage Mater. 50 (2022) 197–224. https://doi.org/10.1016/j.ensm.2022.03.015.

[55] W.J. Chen, B.Q. Li, C.X. Zhao, M. Zhao, T.Q. Yuan, R.C. Sun, J.Q. Huang, Q. Zhang, Electrolyte Regulation towards Stable Lithium-Metal Anodes in Lithium–Sulfur Batteries with Sulfurized Polyacrylonitrile Cathodes, Angew. Chemie - Int. Ed. 59 (2020) 10732–10745. https://doi.org/10.1002/anie.201912701.

[56] B. Ding, L. Shen, G. Xu, P. Nie, X. Zhang, Encapsulating sulfur into mesoporous TiO_2 host as a high performance cathode for lithium-sulfur battery, Electrochim. Acta. 107 (2013) 78–84. https://doi.org/10.1016/j.electacta.2013.06.009.

[57] M. Zlámalová, B. Pitňa Lásková, M. Vinarčíková, M. Zukalová, L. Kavan, Inherent electrochemical activity of TiO_2 (anatase, rutile) enhances the charge capacity of cathodes of lithium-sulfur batteries, J. Solid State Electrochem. 26 (2022) 639–647. https://doi.org/10.1007/s10008-022-05115-z.

[58] J. Li, S. Tang, L. Lu, H.C. Zeng, Preparation of nanocomposites of metals, metal oxides, and carbon nanotubes via self-assembly, J. Am. Chem. Soc. 129 (2007) 9401–9409. https://doi.org/10.1021/ja071122v.

[59] X.Z. Ma, B. Jin, H.Y. Wang, J.Z. Hou, X. Bin Zhong, H.H. Wang, P.M. Xin, S-TiO_2 composite cathode materials for lithium/sulfur batteries, J. Electroanal. Chem. 736 (2015) 127–131. https://doi.org/10.1016/j.jelechem.2014.11.007.

[60] X. Gao, H. Zhu, G. Pan, S. Ye, Y. Lan, F. Wu, D. Song, Preparation and electrochemical

characterization of anatase nanorods for lithium-inserting electrode material, J. Phys. Chem. B. 108 (2004) 2868–2872. https://doi.org/10.1021/jp036821i.

[61] X.Z. Ma, B. Jin, H.Y. Wang, J.Z. Hou, X. Bin Zhong, H.H. Wang, P.M. Xin, S-TiO_2 composite cathode materials for lithium/sulfur batteries, J. Electroanal. Chem. 736 (2015) 127–131. https://doi.org/10.1016/j.jelechem.2014.11.007.

[62] M. Serrapede, U. Savino, M. Castellino, J. Amici, S. Bodoardo, E. Tresso, A. Chiodoni, Li^+ Insertion in Nanostructured TiO_2 for Energy Storage, Materials (Basel). 13 (2020) 21.

[63] S.P. Albu, A. Ghicov, S. Aldabergenova, P. Drechsel, D. LeClere, G.E. Thompson, J.M. Macak, P. Schmuki, Formation of double-walled TiO_2 nanotubes and robust anatase membranes, Adv. Mater. 20 (2008) 4135–4139. https://doi.org/10.1002/adma.200801189.

[64] D. V. Bavykin, J.M. Friedrich, F.C. Walsh, Protonated titanates and TiO_2 nanostructured materials: Synthesis, properties, and applications, Adv. Mater. 18 (2006) 2807–2824. https://doi.org/10.1002/adma.200502696.

[65] Y.J. Bai, C. Gong, N. Lun, Y.X. Qi, Yttrium-modified $Li_4Ti_5O_{12}$ as an effective anode material for lithium ion batteries with outstanding long-term cyclability and rate capabilities, J. Mater. Chem. A. 1 (2013) 89–96. https://doi.org/10.1039/c2ta00048b.

[66] H. Guo, H. Chen, H. Zhang, X. Huang, J. Yang, B. Wang, Y. Li, L. Wang, X. Niu, Z. Wang, Low-temperature processed yttrium-doped $SrSnO_3$ perovskite electron transport layer for planar heterojunction perovskite solar cells with high efficiency, Nano Energy. 59 (2019) 1–9. https://doi.org/10.1016/j.nanoen.2019.01.059.

[67] Y. Zhu, S. An, J. Cui, H. Qiu, X. Sun, Y. Zhang, W. He, Improving the specific capacity of nickel hydroxide nanocrystals: Via yttrium doping for application in hybrid supercapacitors, CrystEngComm. 21 (2019) 4079–4084. https://doi.org/10.1039/c9ce00625g.

[68] N. Li, R. An, Y. Su, F. Wu, L. Bao, L. Chen, Y. Zheng, H. Shou, S. Chen, The role of yttrium content in improving electrochemical performance of layered lithium-rich cathode materials for Li-ion batteries, J. Mater. Chem. A. 1 (2013) 9760–9767. https://doi.org/10.1039/c3ta11665d.

[69] H. Ronduda, M. Zybert, A. Szczęsna, T. Trzeciak, A. Ostrowski, P. Wieciński, W. Wieczorek, W. Raróg-Pilecka, M. Marcinek, Addition of yttrium oxide as an effective way to enhance the cycling stability of $LiCoO_2$ cathode material for Li-ion batteries, Solid State Ionics. 355 (2020) 115426. https://doi.org/10.1016/j.ssi.2020.115426.

[70] A.W. Xu, Y. Gao, H.Q. Liu, The preparation, characterization, and their photocatalytic activities of rare-earth-doped TiO_2 nanoparticles, J. Catal. 207 (2002) 151–157. https://doi.org/10.1006/jcat.2002.3539.

[71] J. wen Shi, J. tang Zheng, P. Wu, Preparation, characterization and photocatalytic activities of holmium-doped titanium dioxide nanoparticles, J. Hazard. Mater. 161 (2009) 416–422. https://doi.org/10.1016/j.jhazmat.2008.03.114.

[72] S. Bouattour, A.M.B. Do Rego, L.F.V. Ferreira, Photocatalytic activity of Li+-Rb+-Y3+ doped or codoped TiO_2 under sunlight irradiation, Mater. Res. Bull. 45 (2010) 818–825. https://doi.org/10.1016/j.materresbull.2010.03.014.

[73] Z. Hamden, D.P. Ferreira, L.F.V. Ferreira, S. Bouattour, Li-Y doped and codoped TiO_2 thin films: Enhancement of photocatalytic activity under visible light irradiation, Ceram. Int. 40 (2014) 3227–3235. https://doi.org/10.1016/j.ceramint.2013.09.114.

[74] Z. Shen, W. Zhang, S. Mao, S. Li, X. Wang, Y. Lu, Tailored Electrolytes Enabling Practical Lithium-Sulfur Full Batteries via Interfacial Protection, ACS Energy Lett. 6 (2021) 2673–2681. https://doi.org/10.1021/acsenergylett.1c01091.

[75] Z. Xiao, Z. Yang, L. Wang, H. Nie, M. Zhong, Q. Lai, X. Xu, L. Zhang, S. Huang, A lightweight TiO_2/Graphene interlayer, applied as a highly effective polysulfide absorbent for fast, long-life lithium-sulfur batteries, Adv. Mater. 27 (2015) 2891–2898. https://doi.org/10.1002/adma.201405637.

[76] K. Han, J. Shen, S. Hao, H. Ye, C. Wolverton, M.C. Kung, H.H. Kung, Free-Standing Nitrogen-doped Graphene Paper as Electrodes for High-Performance Lithium/Dissolved Polysulfide Batteries, ChemSusChem. 7 (2014) 2545–2553. https://doi.org/10.1002/cssc.201402329.

[77] L.C. Yin, J. Liang, G.M. Zhou, F. Li, R. Saito, H.M. Cheng, Understanding the interactions between lithium polysulfides and N-doped graphene using density functional theory calculations, Nano Energy. 25 (2016) 203–210. https://doi.org/10.1016/j.nanoen.2016.04.053.

[78] M. Zhang, C. Yu, C. Zhao, X. Song, X. Han, S. Liu, C. Hao, J. Qiu, Cobalt-embedded nitrogen-doped hollow carbon nanorods for synergistically immobilizing the discharge products in lithium–sulfur battery, Energy Storage Mater. 5 (2016) 223–229. https://doi.org/10.1016/j.ensm.2016.04.002.

Figure captions

Figure 1. Schematic representation of the synthesis of SPAN/Ti-Y composite and the creation of the cathode material with two zones: SPAN/Ti-Y/interlayer, using a two-step coating technique.

Figure 2. a) XRD patterns (A: peaks assigned to TiO_2 anatase polymorphic form according to reference pattern) and b) Raman spectra for commercial TiO_2 (orange) and TiO_2/Y_2O_3 (light blue).c), d) and e) SEM images at 5 µm, 500 nm and 400 nm, respectively for TiO_2/Y_2O_3.

Figure 3. a) TG profiles for sulfur (pink dash line), PAN (purple dash line), TiO_2/Y_2O_3 (green dash line), Control SPAN (blue line) and SPAN/Ti-Y (red line) under oxygen atmosphere, except for sulfur which was performed under nitrogen atmosphere. b) XRD patterns, c) FTIR spectra and d) Raman spectra for SPAN/Ti-Y (red curve) and SPAN/Ti (black curve).

Figure 4. SEM images at a) 5 µm and b) 25 µm and EDS elemental mapping image at c) 25 µm with d) titanium, e) sulfur, f) oxygen and g) carbon of SPAN/Ti-Y composite.

Figure 5. XPS analysis of a) the as-synthesized SPAN/Ti-Y composite and the cell b) discharged after 1 cycle, c) charged after 1 cycle, d) discharged after 2 cycles and e) discharged after 500 cycles at 0.15 C. Color code: black, original data; red, blue, purple, green, light blue and orange, fitted individual peaks.

Figure 6. Potential structure proposed for SPAN/Ti-Y composite. TiO_2/Y_2O_3 particles are not depicted in the scheme since they are physically adsorbed to the matrix.

Figure 7. CV curves for a) the first cycle and b) second cycle for SPAN/Ti-Y/interlayer (red curve), SPAN/Ti (black curve) and TiO_2/Y_2O_3 (green curve). c) Cyclic voltammograms obtained for the first cycle for current collectors coated with TiO_2/Y_2O_3 (green curve) and commercial TiO_2 (orange curve) at 0.1 mV s^{-1}. Orange curve was multiplied by a factor of 2.5.

Figure 8. a) Discharge/charge galvanostatic curves and b) cycling capacity and coulombic efficiency at 0.1 A g^{-1} over 100 cycles for TiO_2/Y_2O_3 and commercial TiO_2. Capacity values are expressed by gram of mixture of metal oxides and by gram of commercial TiO_2, respectively.

Figure 9. Rate capability studies for SPAN/Ti-Y/interlayer and SPAN/Ti with capacity values indicated in a) grams of S&TiO_2/Y_2O_3 and S&TiO_2 and b) grams of composite.

Figure 10. a) Cycling performance for SPAN/Ti-Y/interlayer (red) and SPAN/Ti (black) at 0.45 C (0.6 A g^{-1}) and coulombic efficiency for SPAN/Ti-Y/interlayer and b) Cycling performance for SPAN/Ti-Y/interlayer (red) and SPAN/Ti (black) at 3.00 C (3.9 A g^{-1}) and coulombic efficiency for SPAN/Ti-Y/interlayer.

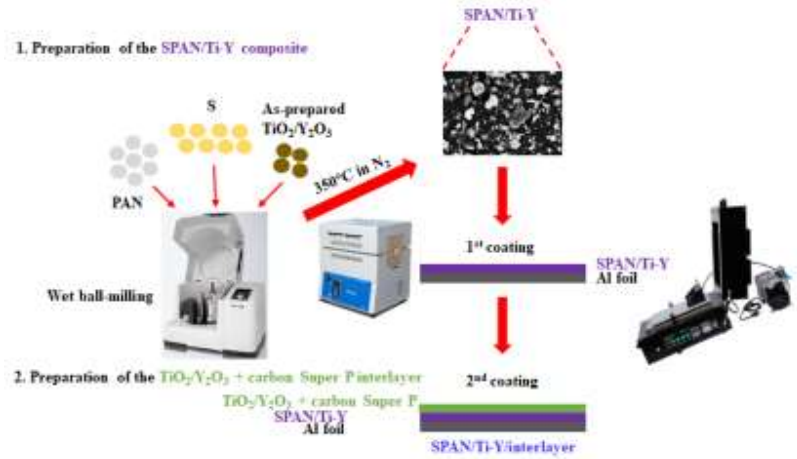

Figure 1

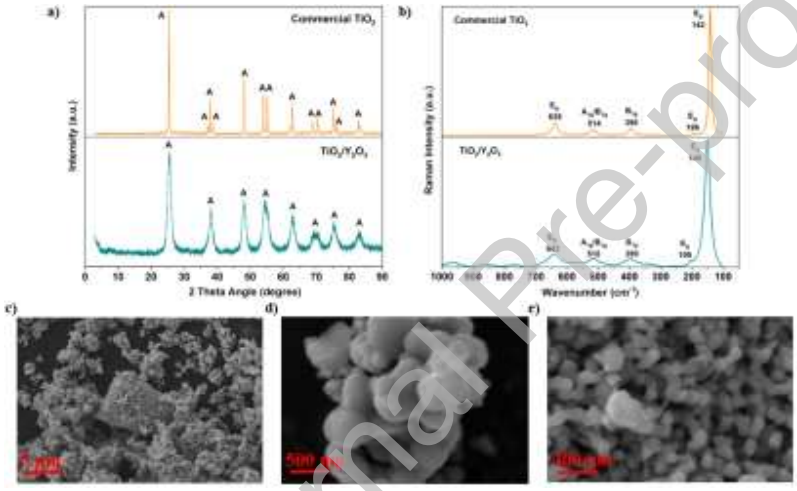

Figure 2

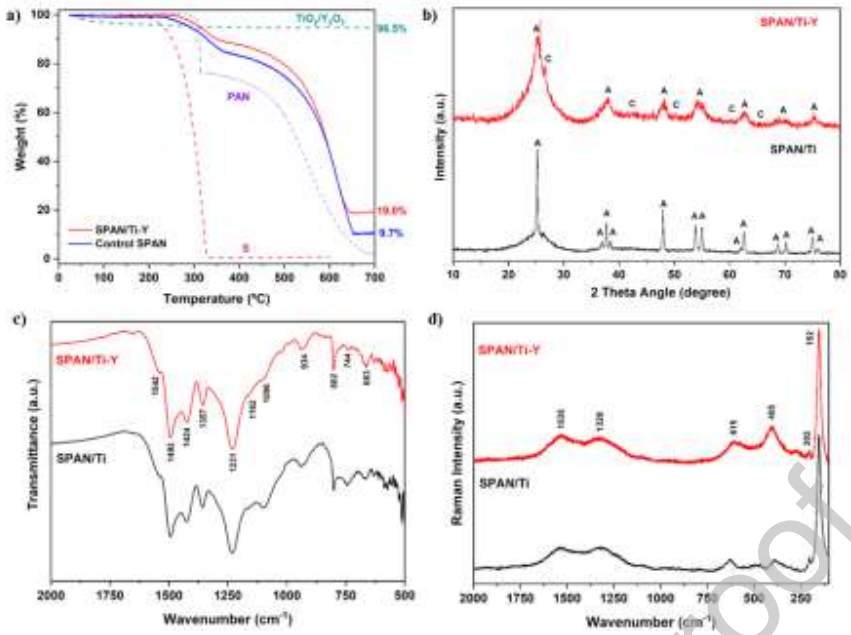

Figure 3

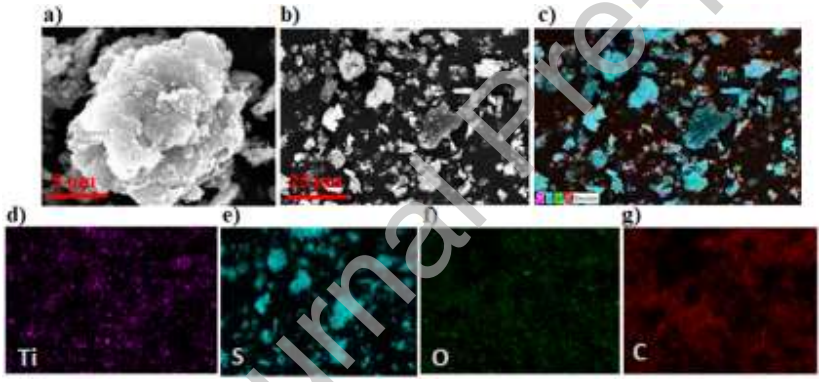

Figure 4

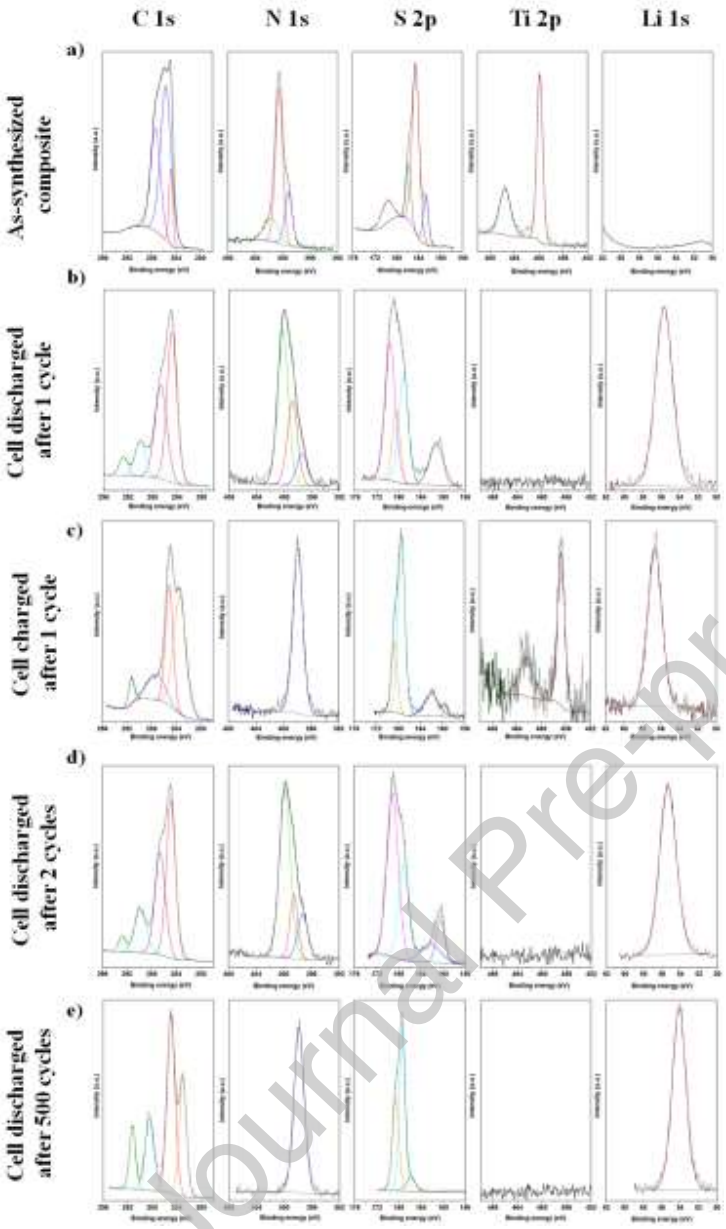

Figure 5

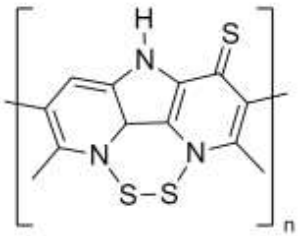

Figure 6

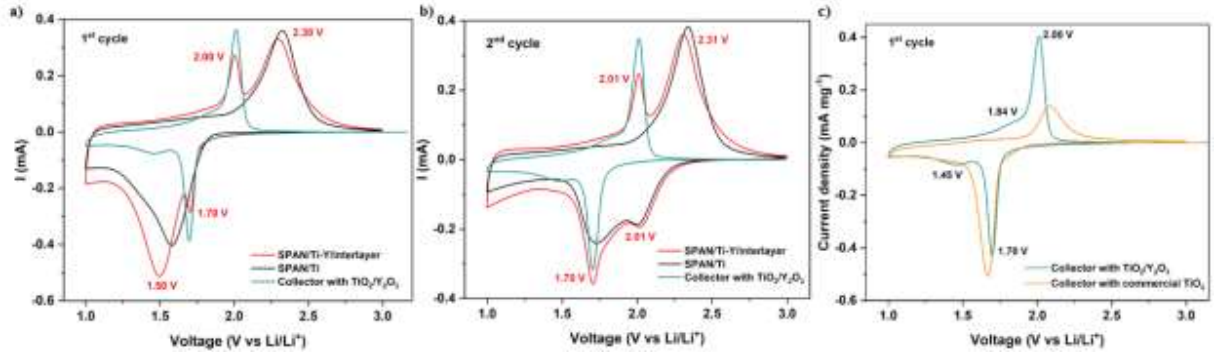

Figure 7

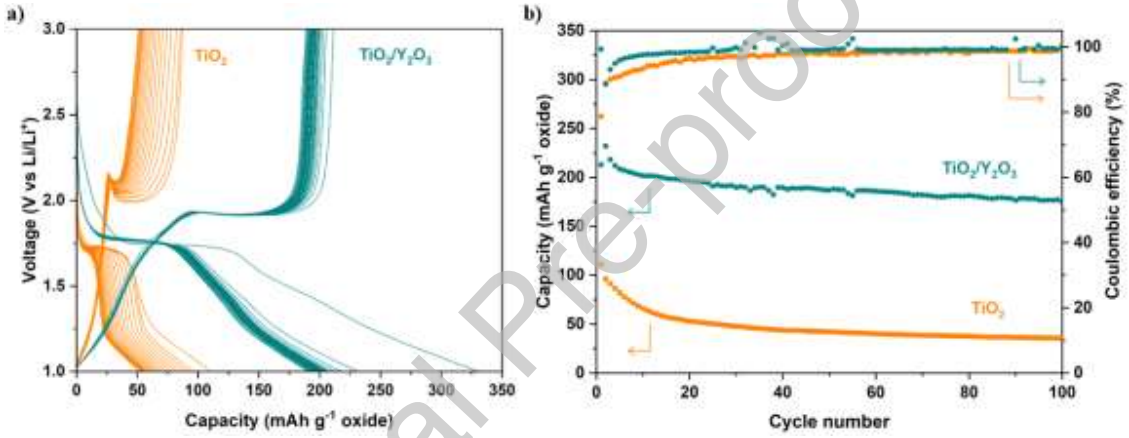

Figure 8

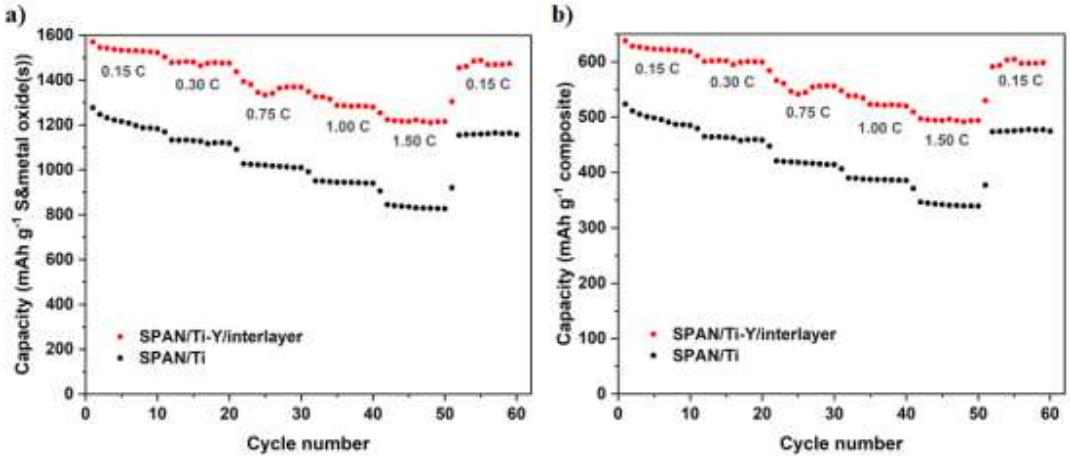

Figure 9

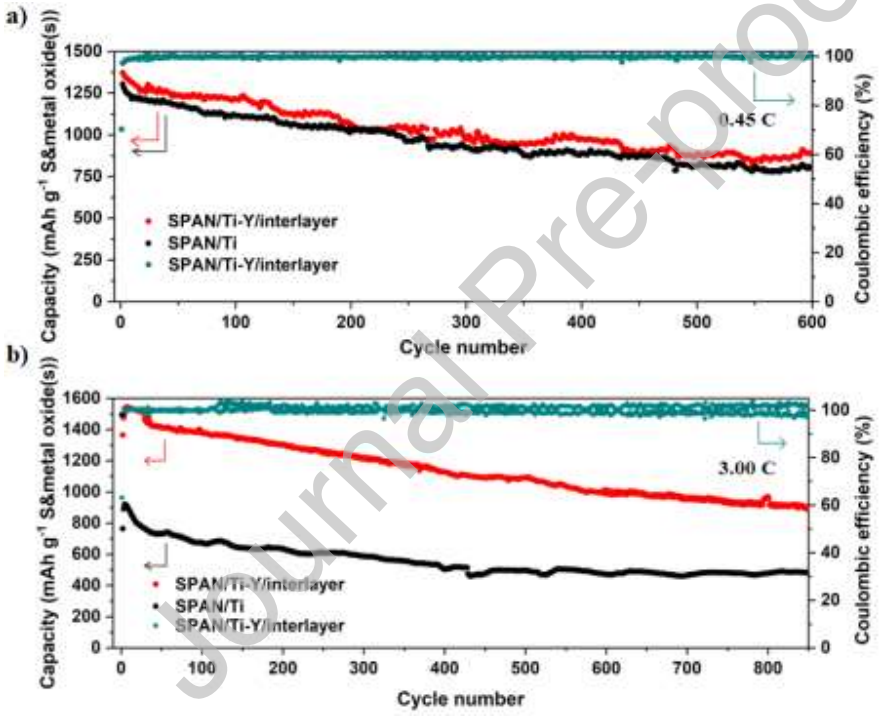

Figure 10

Credit Author Statement

Ana L. Páez Jerez: Methodology, Data collection, Formal analysis, Investigation, Writing – original draft, Writing – review & editing. **Maria L. Vera:** Conceptualization, Formal Analysis. **Edgardo L. Sham:** Investigation. **Alvaro Y. Tesio**: Conceptualization, Writing – review, Funding acquisition. **Victoria Flexer:** Conceptualization, Writing – review & editing, Funding acquisition. All authors have read and agreed to the published version of the manuscript.

Declaration of interests

☒The authors declare that they have no known competing financial interests or personal relationships that could have appeared to influence the work reported in this paper.

☐The authors declare the following financial interests/personal relationships which may be considered as potential competing interests: